Chapter 31 – NUMERICAL SOLUTIONS FOR THE VFE-2 CONFIGURATION ON UNSTRUCTURED GRIDS AT DLR, GERMANY

by

Andreas Schütte and Heinrich Lüdeke

31.1 INTRODUCTION

The flow field around delta wing configurations with sharp leading edges is well known from former experimental and theoretical studies as well as the treatment of flow simulations using high fidelity numerical methods. Within the last years several experimental and numerical investigations are published focusing on the flow topology, Re- and Mach number effects as well as on transition behavior of the vortex dominated flow field around sharp leading edges. This is described in detail within publications of the US/European Vortex Flow Experiment [31-1]-[31-5]. The flow around a sharp leading edge delta wing is characterized by primary vortices initially separating directly at the apex even at small angles of attack. The shear layer rolls up to a pair of primary vortices over the wing. The secondary vortices occur due to the separation of the flow of the primary vortex interacting with the boundary layer on the wing surface, as depicted in Figure 31-1. The strength and position at the primary and secondary vortices are mainly influenced by the inflow velocity, angle of attack and the sweep angle of the delta wing [31-6] [31-7]. The vortex flow under turbulent flow conditions is fairly independent of the Reynolds number for sharp leading edge delta wings whereas under laminar flow conditions the Reynolds number affects the position and strength of the vortices as well as the vortex topology over the wing [31-8].

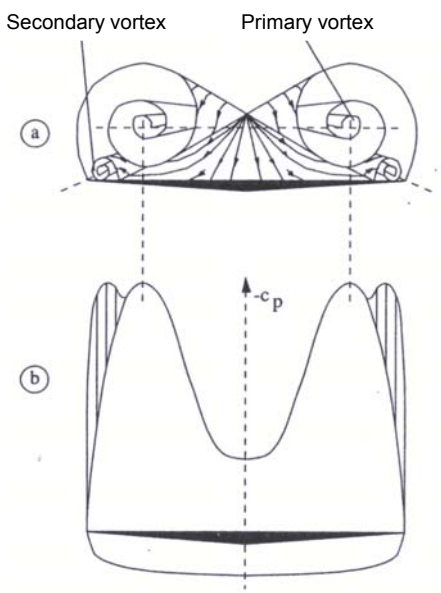

Figure 31-1: Schematic View of the Flow over a Sharp Edged Delta Wing – (a) Vortex Formation; (b) Pressure Distribution in a Cross Section [31-6].

Recent and future fighter configurations are mainly delta wing configurations with rounded leading edges. The flow around delta wing configurations with rounded leading edges is still not entirely understood. Therefore a second Vortex Flow Experiment – VFE-2 with the RTO/AVT-113 was established, focusing on the flow around delta wing configurations with rounded leading edges [31-9]. Several experimental data sets were provided and generated within the RTO/AVT-113 task group regarding on a 65° swept delta wing with sharp and different rounded leading edges. The experimental data base is used to expand the knowledge about the flow topology and flow physics and to validate computational codes. This paper is focusing on the flow topology around the VFE-2 delta wing with medium rounded leading edges at different Reynolds numbers and angles of attack.

The motivation for using an unstructured grid approach is intended by the simulation of complex realistic fighter configurations especially by taking all control devices and storages into account. The presented investigation is intended as a test to predict the correct physics of the highly complex flow topology of delta wings with rounded leading edge by an unstructured code.

31.2 NUMERICAL APPROACH

31.2.1 CFD Solver TAU

The flowfield is predicted with the TAU-Code, a CFD tool developed by the DLR Institute of Aerodynamics and Flow Technology [31-10][31-12]. The TAU-Code solves the compressible, three-dimensional, time-accurate Reynolds-Averaged Navier-Stokes equations by using a finite volume formulation. The code is based on a hybrid unstructured-grid approach making use of the advantages of prismatic grids for the resolution of viscous shear layers near walls, and the flexibility in grid generation offered by unstructured grids. The grids used for simulations in this paper were created with the hybrid grid generator Centaur, developed by Centaur Soft [31-13]. A dual-grid approach is used in order to get a second-order cell-vertex based scheme. The TAU-Code consists of several different modules, among which are:

- The Preprocessor module, which uses the information of the initial grid to create a dual-grid and the coarser grids for multi-grid.
- The Solver module, which performs the flow calculations on the dual-grid.
- The Adaptation module, which refines and de-refines the grid in order to capture flow phenomena like vortex structures and shear layers near viscous boundaries, among others.

The Solver module contains several upwind schemes, as well as central schemes with artificial dissipation, which are used for the spatial discretization. For simulations of turbulent flows, various modifications of the one-equation Spalart-Allmaras and several two-equation turbulence models are implemented. For steady computations either an explicit Runge-Kutta type time-stepping or an implicit LU-SSOR-scheme are used in combination with the multi-grid technique to advance the solution in time. For time-accurate simulations an implicit dual-time stepping approach is used.

Several one- and two equation turbulence models are available for steady simulations. In the presented RANS-simulations the original one-equation Spalart-Allmaras (SA) [31-14] model and the two equations Wilcox k-ω model [31-15] are used which are briefly described in the following. The SA model defines the eddy viscosity field as:

$$\mu_t = \rho \nu_t = \rho \tilde{\nu} f_{v1}$$

with ρ as the density, ν_t as the turbulent kinematic viscosity and f_{v1} as a near wall-function that guarantees linearity of the turbulent transport quantity in the vicinity of walls. The distribution of the transport quantity $\tilde{\nu}$ is determined by the solution of a transport equation:

$$\frac{D(\rho\tilde{\nu})}{Dt} = \underbrace{c_{b1}\tilde{S}\rho\tilde{\nu}}_{P} - \underbrace{C_{w1}f_w\rho\left(\frac{\tilde{\nu}}{d}\right)^2}_{D} + \underbrace{\frac{\rho}{\sigma}\left\{\nabla\left[(\nu+\tilde{\nu})\nabla\tilde{\nu}\right] + c_{b2}(\nabla\tilde{\nu})^2\right\}}_{DF}$$

with d as the wall distance. This transport equation contains phenomenological models of production P, destruction D and diffusion DF which are described in the literature [31-14]. In the production term P a modified vorticity $\tilde{S}$ appears that maintains the linear behavior of the model near walls. The different model constants are determined by experimental data and analytical solutions and are well known for turbulent flow fields [31-14].

The k-ω model equations [31-15], including the cross-diffusion term C_D, are given by:

$$\frac{\partial\rho k}{\partial t} + \frac{\partial(\rho k V_j)}{\partial x_j} = P_k - \beta^*\rho\omega k + \frac{\partial}{\partial x_j}\left((\mu+\sigma_\omega\mu_t)\frac{\partial k}{\partial x_j}\right)$$

$$\frac{\partial\rho\omega}{\partial t} + \frac{\partial(\rho\omega V_j)}{\partial x_j} = P_k - \beta^*\rho\omega^2 + \frac{\partial}{\partial x_j}\left((\mu+\sigma_\omega\mu_t)\frac{\partial\omega}{\partial x_j}\right) + C_D$$

with ρ the density, $\tilde{V}$ the velocity vector, μ the molecular-viscosity coefficient, k the turbulent kinetic energy, ω the specific turbulent dissipation and $\mu_t = \rho k/\omega$ the eddy-viscosity coefficient. The production and cross-diffusion terms are given by Wilcox as well as the six closure coefficients: α_ω, β^*, β, σ_k, σ_ω and σ_d , also provided by Wilcox [31-15].

31.3 EXPERIMENTAL DATA

For the validation of the numerical simulation software, various wind-tunnel data sets are provided by NASA within the RTO/AVT-113 task group [31-16]. Additionally wind tunnel experiments were carried out with a 2/3 scaled wind tunnel model loaned by NASA to DLR [31-17]. These wind tunnel experiments consist of pressure distribution measurements using PSI pressure taps and PSP-"Pressure Sensitive Paint" [31-18] as well as measurements of the flow field via PIV – "Particle Image Velocimetry" [31-19]. Figure 31-2 shows the NASA wind tunnel model in the NTF wind tunnel at NASA Langley.

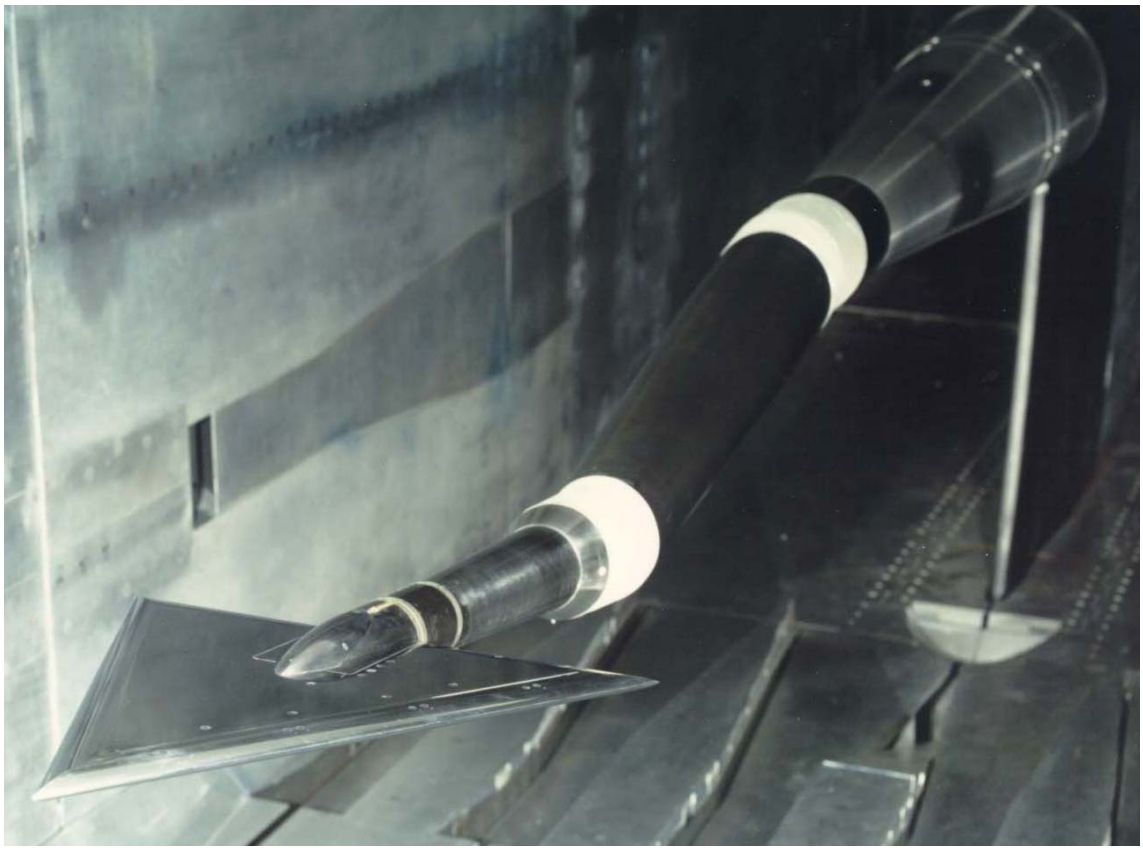

Figure 31-2: NASA 65° Delta Wing in the NTF-Wind Tunnel at NASA-Langley Research Center. Source: J.M. Luckring, NASA Langley [31-16].

31.3.1 Flow Topology

For the validation of the RANS solver TAU, the results of the numerical simulations are compared against data collected from various experimental simulations. Figure 31-3 shows the pressure distribution over the delta wing with medium rounded leading edge radius. The measurement is done by using PSP at a Mach number of M = 0.4, an angle of attack of α = 13.3° and a Reynolds number of Re = 3 x 10^6. Two suction traces can be observed on the upper side of the delta wing. A weaker inner suction trace starting from the apex and a stronger outer suction trace initiates at approximately 50% chord length.

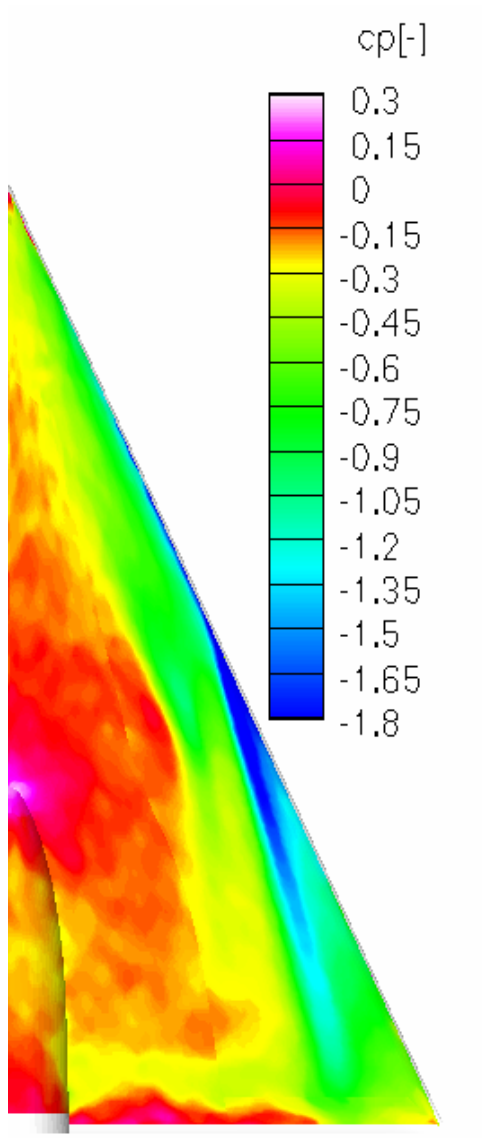

Figure 31-3: Pressure Distribution on the Upper Side of the Wing Using PSP-"Pressure Sensitive Paint" – M = 0.4, Re = 3 x 10^6, α = 13.3° [31-17].

Figure 31-4 shows a PIV result under the same flow conditions described before. The measurement setup is shown in Figure 31-5. The PIV result in Figure 31-4 shows two vortices possessing the same rotational direction. The topology can be described as follows. Because of the leading edge geometry with rounded leading edges the wing tip can be assumed as a blunt body. The flow around the leading edge is initially attached. Further downstream the flow separates and the inner vortex is generated. Regarding the ratio between leading edge radius and wing span the leading edge is getting sharper relative to the downstream position. This leads eventually to a separation of the shear layer further downstream at the leading edge and the outer vortex is generated.

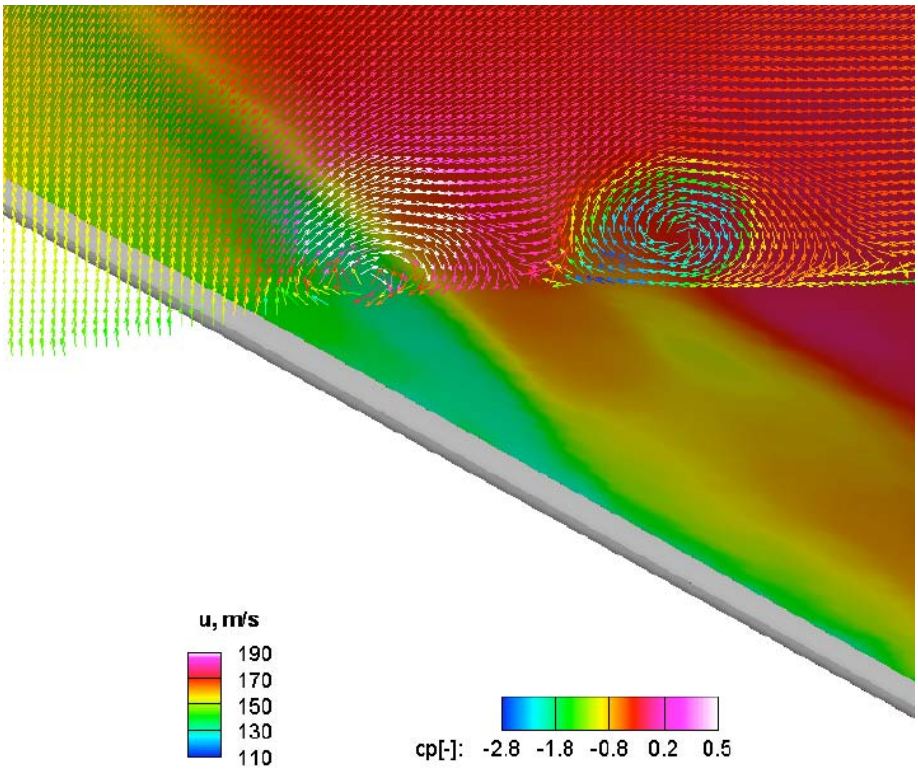

Figure 31-4: Pressure Distribution on the Upper Surface and PIV Measurement at x/c_{ref} = 0.6 – M = 0.4, Re = 3 x 10^6, α = 13.3° [31-19].

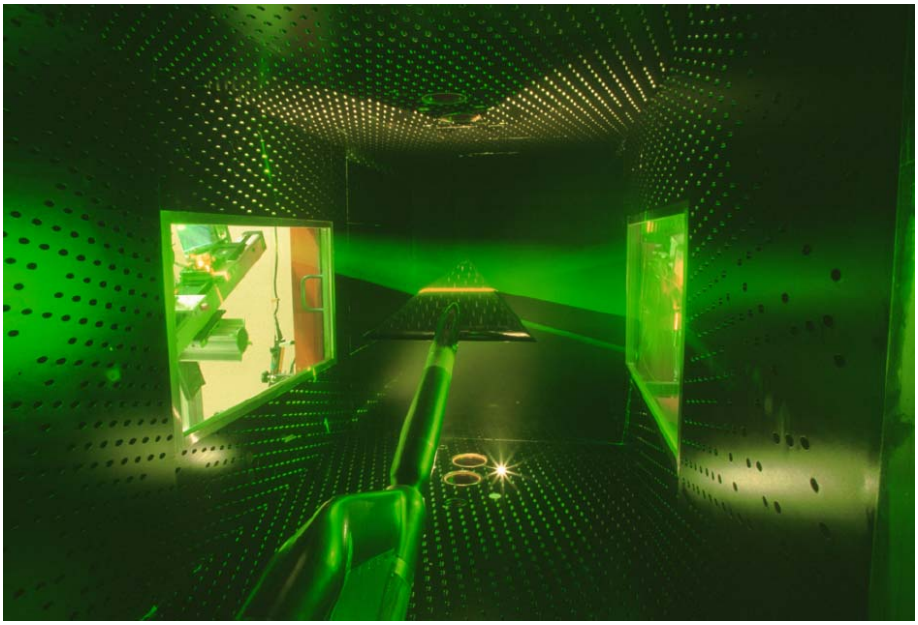

Figure 31-5: Model Setup for PIV Measurements in the TWG-"Transonic Wind Tunnel Göttingen". The laser light sheet can be observed at approximately 50% chord length [31-19].

31.4 NUMERICAL RESULTS

The capability to predict the flow topology with the TAU-Code shall be shown by the following numerical results. Furthermore Reynolds number and Mach number effects on the flow topology around the delta wing will be analyzed and discussed.

31.4.1 Computational Grid

In Figure 31-6 the grid topology of the computational model is depicted. For the numerical simulation a half configuration is used. The sting is modeled up to 30% chord length behind the trailing edge. Figure 31-7 shows a slice through the computational mesh at 90% chord length. For all calculations a pre-refined grid is used for which the area where the vortices occur is refined from the apex up to 10% chord length behind the trailing edge of the wing. The boundary layer is resolved by twenty prismatic layers which is sufficient since the flow is vortex dominated in the region of interest and an extensive resolution of the outer boundary layer is not necessary [31-20].

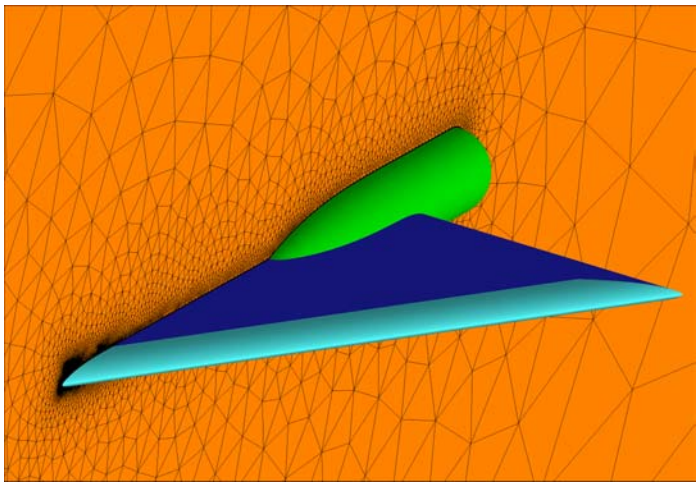

Figure 31-6: Numerical Model Topology and Computational Grid of the Symmetry Plane.

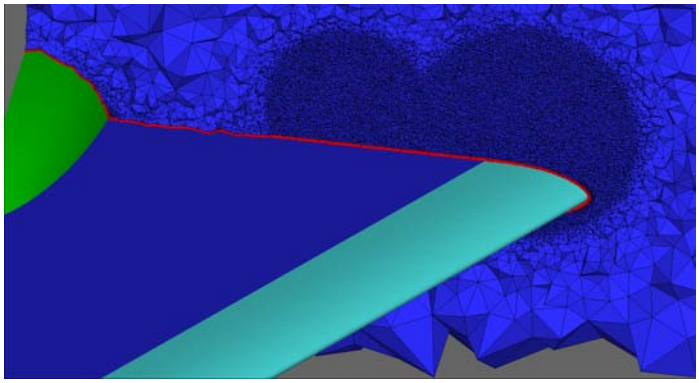

Figure 31-7: Slice through the Computational Grid Close to the Trailing Edge Regarding the Prismatic Layer in Red and the Pre-Refined Grid Area at the Outer Wing in Dark Blue.

For the RANS calculations the Wilcox k-ω turbulence model and the one equation Spalart-Allmaras turbulence model is used. For the time integration of the steady state simulations an implicit Backward Euler time-stepping scheme is chosen. For the RANS calculations a central classic and matrix dissipation scheme is used and fully turbulent flow is assumed for all calculations.

Figure 31-8 shows the simulation result at an angle of attack of $\alpha = 13.3°$ at a Reynolds number of 3×10^6. Comparing the flow topology with the PIV measurements in Figure 31-4 it can be observed that the two vortices are predicted correctly by the simulation. An inner vortex and an outer vortex occur rotating in the same direction.

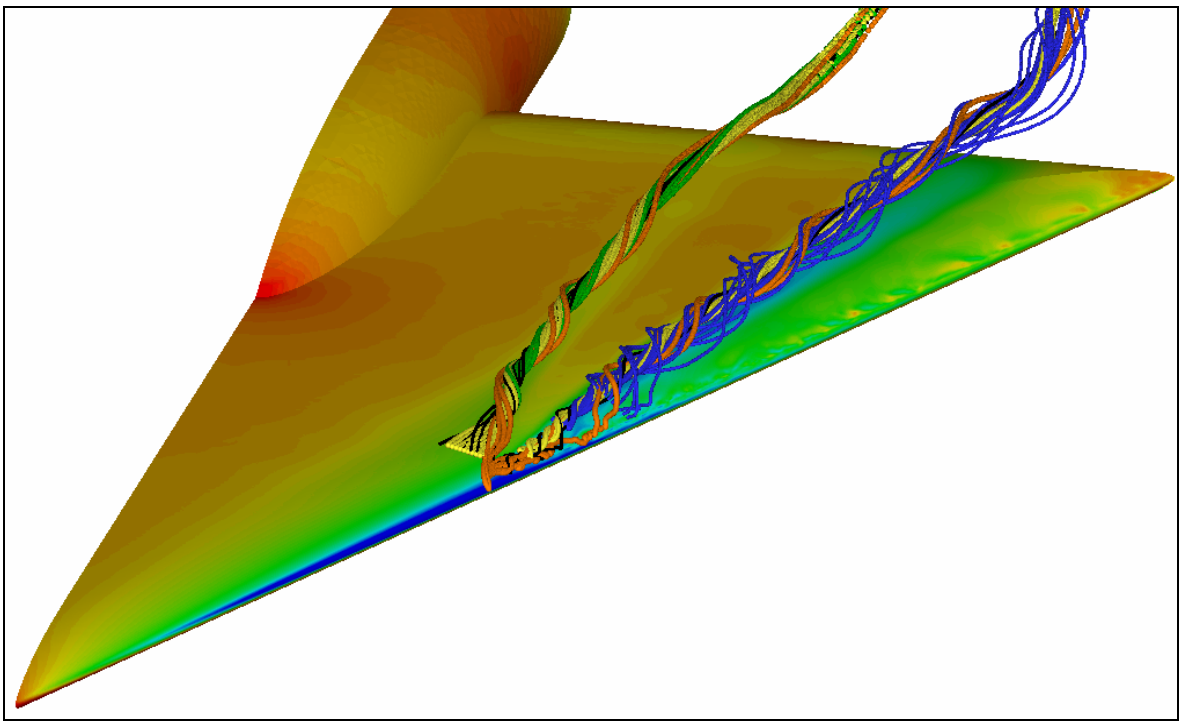

Figure 31-8: Flow Topology on the Upper Surface of the 65° Delta Wing with Medium Radius Leading-Edge. RANS calculation at M = 0.4, Re = 3 x 10^6, α = 13.3°.

31.4.2 Wilcox k-ω Calculations

Figure 31-9 and Figure 31-10 show a comparison of the pressure distributions between CFD calculation and PSP measurement. The free stream conditions are M = 0.4 at an angle of attack of $\alpha = 13.3°$. Figure 31-9 shows the surface pressure distribution at a Reynolds number of 2×10^6 while Figure 31-10 shows the pressure distribution at 3×10^6 Reynolds number.

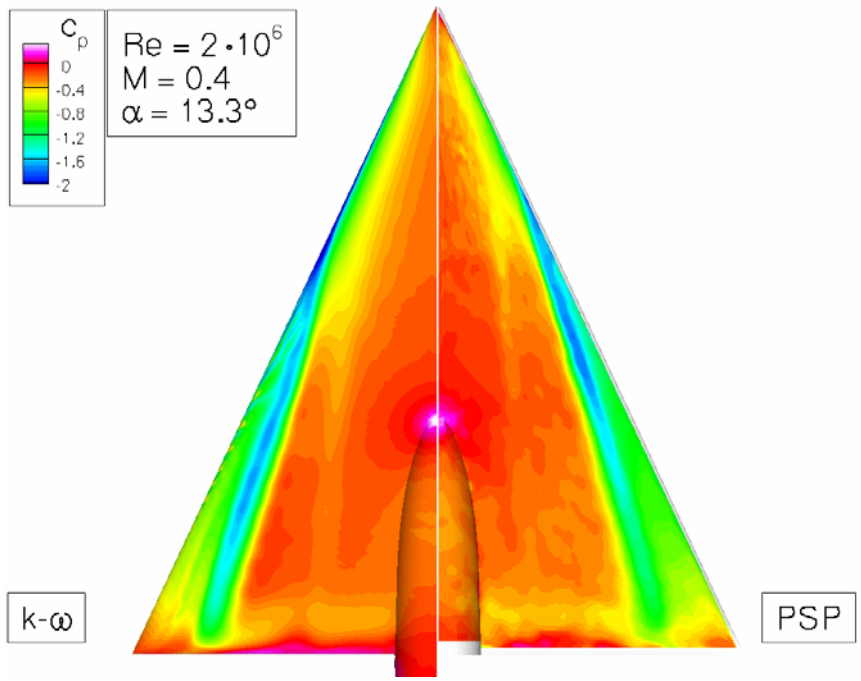

Figure 31-9: Comparison of Pressure Distribution at Angle of Attack α = 13.3° (Left: CFD Calculation Using the k-ω Turbulence Model; Right: PSP Measurement – M = 0.4, Re = 2 x 10^6).

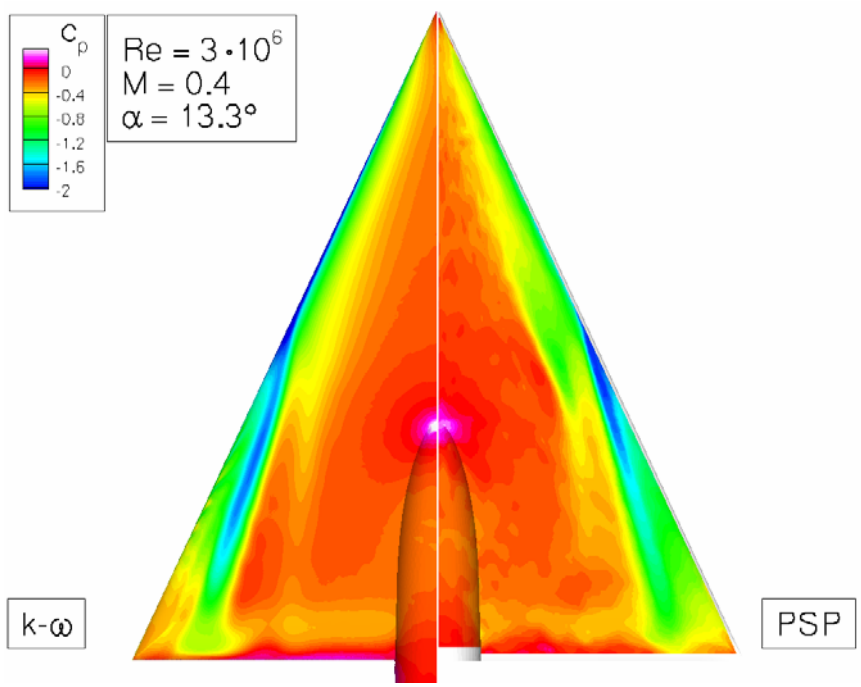

Figure 31-10: Comparison of Pressure Distribution at Angle of Attack α = 13.3° (Left: CFD Calculation Using the k-ω Turbulence Mode; Right: PSP Measurement – M = 0.4, Re = 3 x 10^6).

In both cases the two equation k-ω turbulence model is used. It is seen that for both Reynolds numbers the flow pattern of the inner and outer vortex is represented by the CFD calculation. Furthermore a Reynolds number effect is captured by the simulation. As in the experiment it is visible that the outer vortex is generated further downstream, enhancing with the Reynolds number and the suction pattern of the inner vortex affects the pressure distribution on the surface further towards the trailing edge. In the case of 2 x 10^6 Reynolds number it can be observed that the outer vortex occurs too far downstream in comparison with the experiment. In the case of 3 x 10^6 Reynolds number the location of the beginning of the outer vortex fits quite well with the experiment. For both Reynolds numbers the inner vortex occurs too far outboard. Concerning the strength of the inner and outer vortex it can be observed that in the 2 x 10^6 Reynolds number case the suction peak of the outer vortex is stronger than in the experiment whereas the suction pattern is going further towards the trailing edge. The same can be observed for the Reynolds number of 3 x 10^6. The strength of the inner vortex at 3 x 10^6 Reynolds number can be assumed to be under predicted by the simulation.

Taking a view on the quantities in Figure 31-11 and Figure 31-12 the results of the pressure distributions at five different stages x = const. planes are compared with the experiment taking from PSI pressure measurements. As discussed before the effect of the too far downstream generated outer vortex is visible in Figure 31-11 for a Reynolds number of 2 x 10^6. Whereas in the experiment at x = 0.4 the pressure distribution represents a vertical flow, the pressure distribution in the simulation is more or less attached at the leading edge.

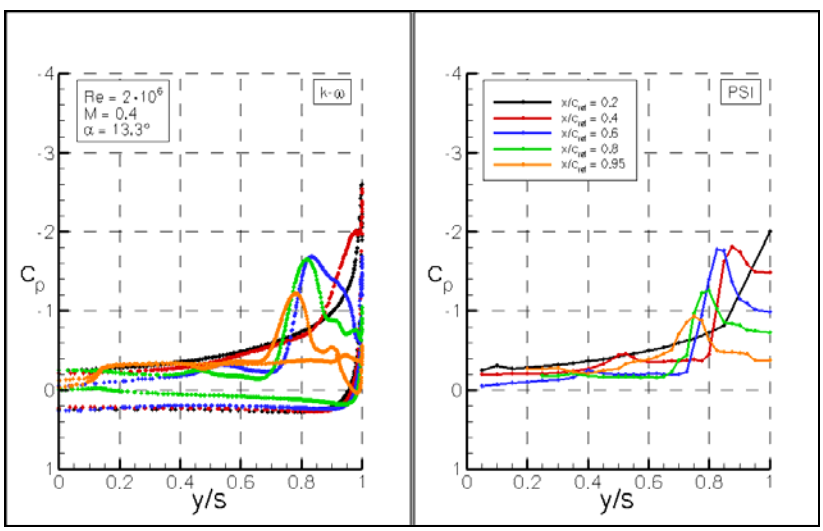

Figure 31-11: Comparison of Pressure Distribution at Angle of Attack α = 13.3° (Left: PSI Measurement; Right: CFD Calculation Using the k-ω Turbulence Model – M = 0.4, Re = 2 x 10^6).

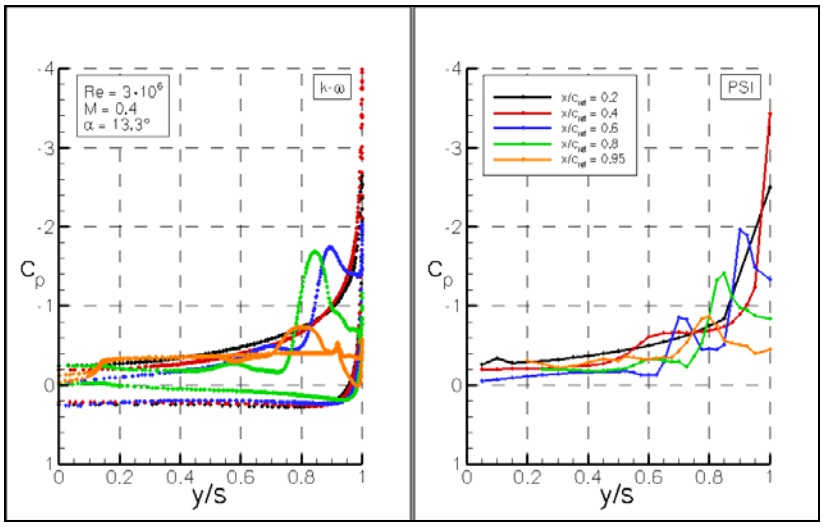

Figure 31-12: Comparison of Pressure Distribution at Angle of Attack α = 13.3° (Left: PSI Measurement; Right: CFD Calculation Using the k-ω Turbulence Model – M = 0.4, Re = 3 x 10^6).

This results in higher suction peaks of the outer vortex further downstream in the simulation in comparison with the experiment, since the outer vortex is passing the x = const. stages further downstream within the simulation. For the 3 x 10^6 Reynolds number case in Figure 31-12 the flow in the experiment is attached till 40% chord length, while the suction peak at the leading is overpredicted in the simulation. The position of the outer vortex is predicted correctly by the simulation which can be observed by the correct positions of the spanwise suction peaks. For both cases the inner vortex suction peaks are predicted too weak independent of the downstream position. For both Reynolds number cases the inner vortex is represented too late in the pressure distribution. For both investigated Reynolds numbers the inner vortex can be detected by a small suction peak at 40% chord length in the experiment where as in the simulation the pressure distribution represents attached flow. Regarding the pattern of the pressure distribution towards the apex in Figure 31-9 and Figure 31-10 higher suction peaks can be observed in the experiment in comparison with the simulation. This might be a result of the weakness of the inner vortex because it occurs later than in the experiment or the vortex generating process starts later respectively.

31.4.3 Spalart-Allmaras Calculations

As identified above there are weaknesses concerning the use of the k-ω turbulence model. Because of this further investigations are carried out using the one equation Spalart-Allmaras (SA) turbulence model. In Figure 31-13 and Figure 31-14 the comparison between the measured pressure distribution with PSP on the right hand side and CFD simulation on left hand side is shown for two Reynolds numbers. It can be observed, that in comparison with the k-ω simulations the suction peaks of the inner and outer vortex in case auf the simulation using the Spalart-Allmaras turbulence model are much stronger. This fits significantly better with the experimental data for both Reynolds number cases (2 x 10^6 and 3 x 10^6). Whereas in the k-ω simulations the outer vortex is predicted for both Reynolds numbers further downstream than in the SA simulations the outer vortex is generated upstream of the experimental position. This causes the position of the inner vortex in the SA cases to be more inboard even though the suction peak of the inner vortex is predicted much better than using the k-ω turbulence model.

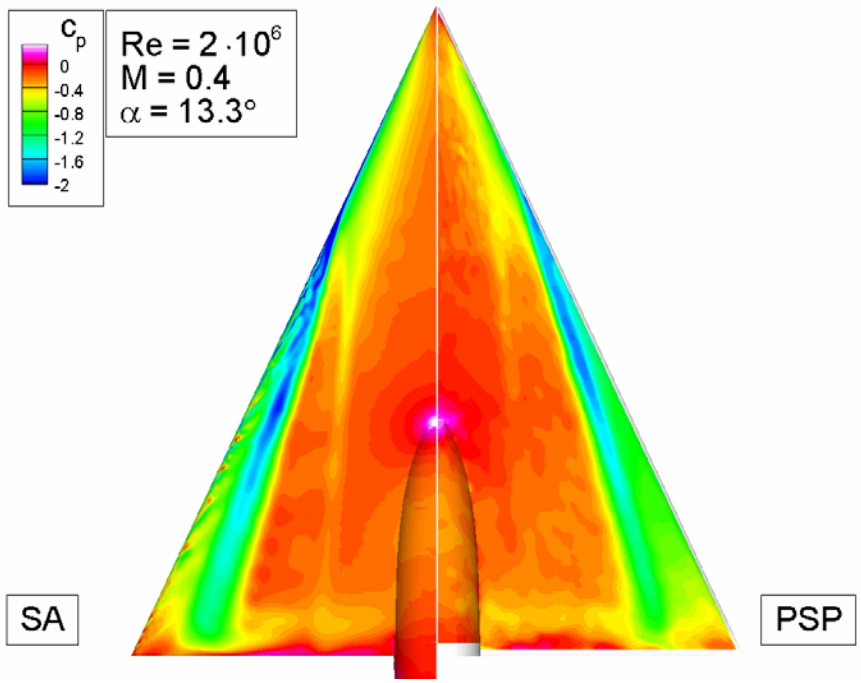

Figure 31-13: Comparison of Pressure Distribution at Angle of Attack α = 13.3° (Left: CFD Calculation Using the Spalart-Allmaras Turbulence Model: Right: PSP Measurement – M = 0.4, Re = 2 x 10^6).

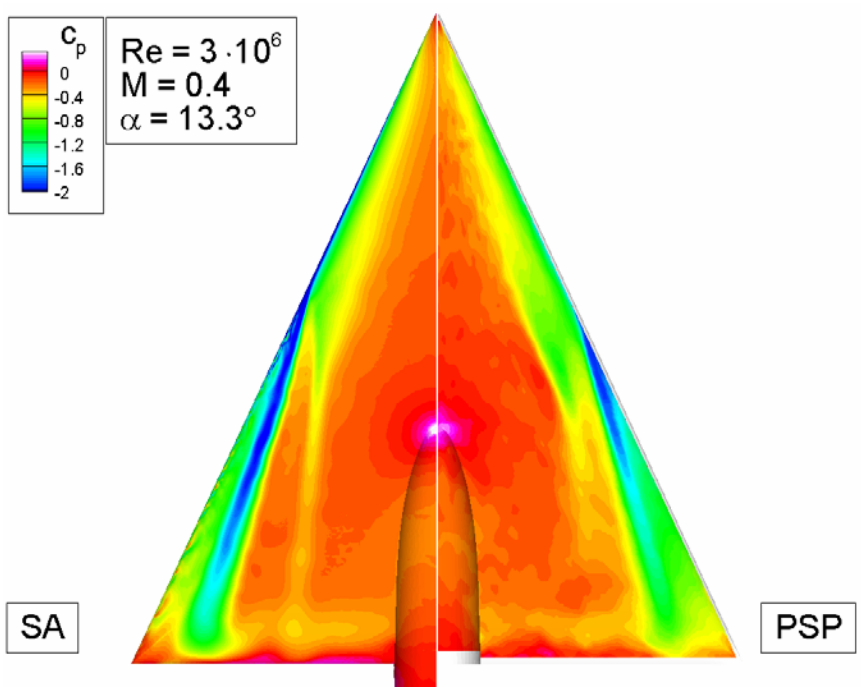

Figure 31-14: Comparison of Pressure Distribution at Angle of Attack α = 13.3° (Left: CFD Calculation Using the Spalart-Allmaras Turbulence Model; Right: PSP Measurement – M = 0.4, Re = 3 x 10^6).

This can be verified by looking at the results in Figure 31-15 and Figure 31-16. Similar to Figure 31-11 and Figure 31-12 the calculation results are compared with measured PSI data at several x = const. positions. The suction peak of the inner vortex is visible better predicted for the 3 x 10^6 Reynolds number case, see Figure 31-16 at $x/c_{ref} = 0.6$. But even for the SA turbulence model it is seen that the inner vortex occurs too far downstream comparing the pressure distribution at $x/c_{ref} = 0.4$ in Figure 31-16. For the 2 x 10^6 case in Figure 31-15 the inner vortex is generated at the correct position and can be observed in the pressure distribution at $x/c_{ref} = 0.4$ but stronger and more outboard than in the experiment. The overall results show a much better agreement with the experiment using the SA than the k-ω turbulence model.

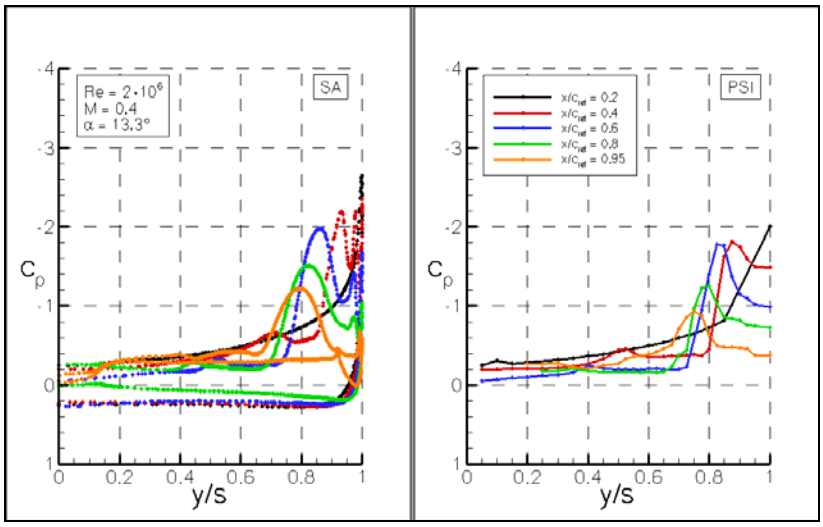

Figure 31-15: Comparison of Pressure Distribution at Angle of Attack α = 13.3° (Left: PSI Measurement; Right: CFD Calculation Using the Spalart-Allmaras Turbulence Model – M = 0.4, Re = 2 x 10^6).

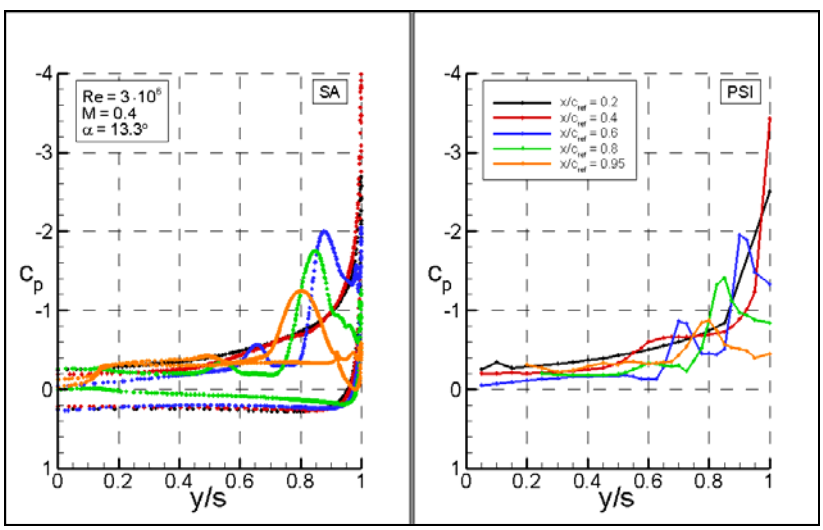

Figure 31-16: Comparison of Pressure Distribution at Angle of Attack α = 13.3° (Left: PSI Measurement; Right: CFD Calculation Using the Spalart-Allmaras Turbulence Model – M = 0.4, Re = 3 x 10^6).

31.4.4 Sensitivities

Within these section two main sensitivities influencing the flow topology on the upper surface of the delta wing will be discussed. These are the influence of the Reynolds number and the angle of attack. In Figure 31-17 the Reynolds number effect is shown. Three different simulations at Re = 1 x 10^6, 2 x 10^6 and 3 x 10^6 are depicted. For all three simulations the k-ω turbulence model is used. The effect of the Reynolds number matches with former observations. By increasing the Reynolds number the outer and inner vortex occurs further downstream and the suction peak of the inner vortex is shifted consequently towards the trailing edge.

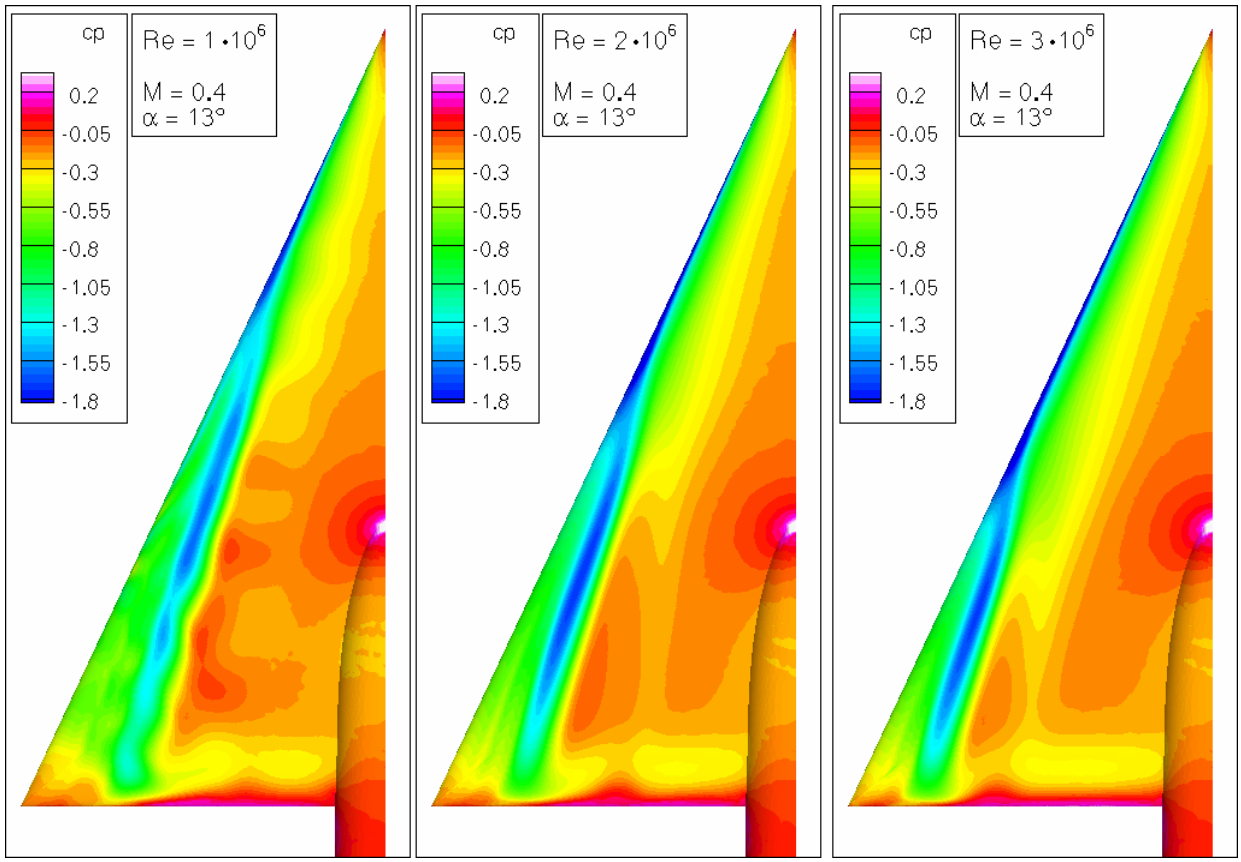

Figure 31-17: CFD Simulation with the DLR TAU-Code. Comparison of pressure distribution at an angle of attack of α = 13.0° – M = 0.4 and three different Reynolds numbers.

Figure 31-18 shows the effect of the angle of attack on the upper side pressure distribution of the delta wing. On the left hand side the simulation at an angle of attack of α = 13.3° is shown and on the right hand side the result at α = 13.0°. Both simulations are done by using the Spalart-Allmaras turbulence model. This small difference of Δα = 0.3° results in significant differences of the vortex locations. By enhancing α the inner and outer vortex are generated further upstream and the location of the inner vortex moves inboard. This is visible even better in Figure 31-19 comparing the suction peaks of the inner vortex at $x/c_{ref} = 0.6$.

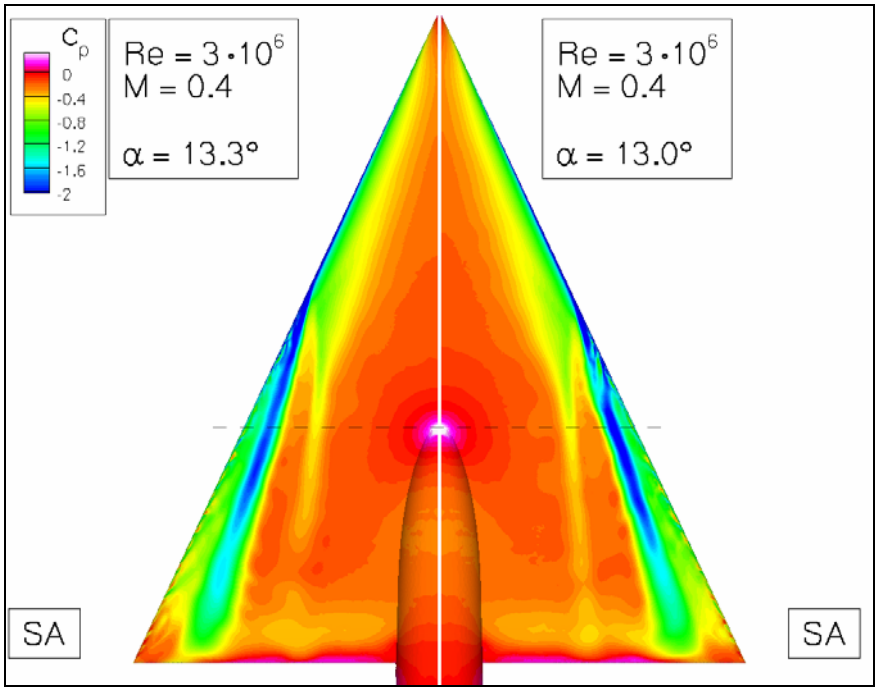

Figure 31-18: Comparison of Surface Pressure Distribution at an Angle of Attack of α = 13.3° and α = 13.0°. CFD calculation using the Spalart-Allmaras turbulence model – M = 0.4, Re = 3 x 10^6.

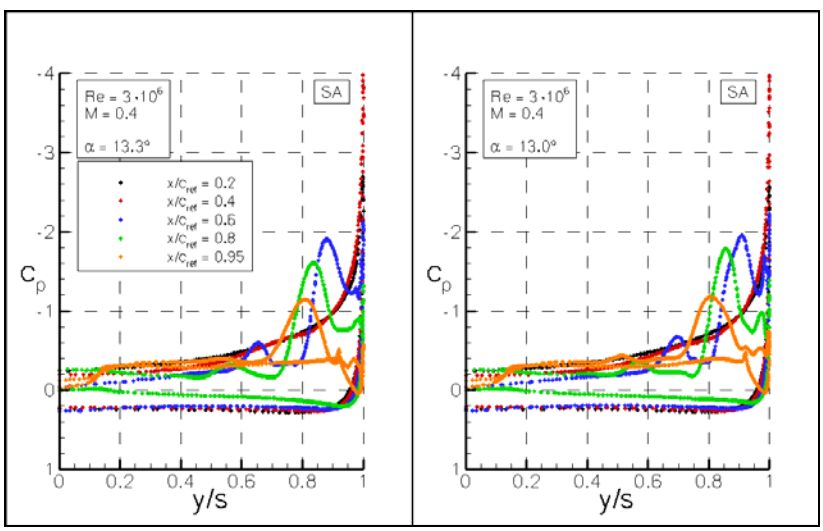

Figure 31-19: Comparison of Pressure Distribution at Slices x = const at an Angle of Attack of α = 13.3° and α = 13.0°. CFD calculation using the Spalart-Allmaras turbulence model – M = 0.4, Re = 3 x 10^6.

31.4.5 Flow Physics

The flow topology on the upper wing surface of the delta wing and the mechanism of the generation of the inner and outer vortex will be discussed in the following section. Figure 31-20 shows the surface friction lines

for the 3 x 10^6 Reynolds number case at an angle of attack of α = 13.3°. Figure 31-20 shows the same calculation, already discussed for Figure 31-14 and Figure 31-16. The red dashed lines assign the trajectories of the vortices on the upper wing side. The most central one is the inner primary vortex, the next one outboard is the outer primary vortex and finally the secondary vortex of the outer primary vortex is visible near the leading edge. Furthermore the attachment lines of the primary outer vortex as well as the separation lines of the inner and outer primary vortex and the secondary vortex are depicted.

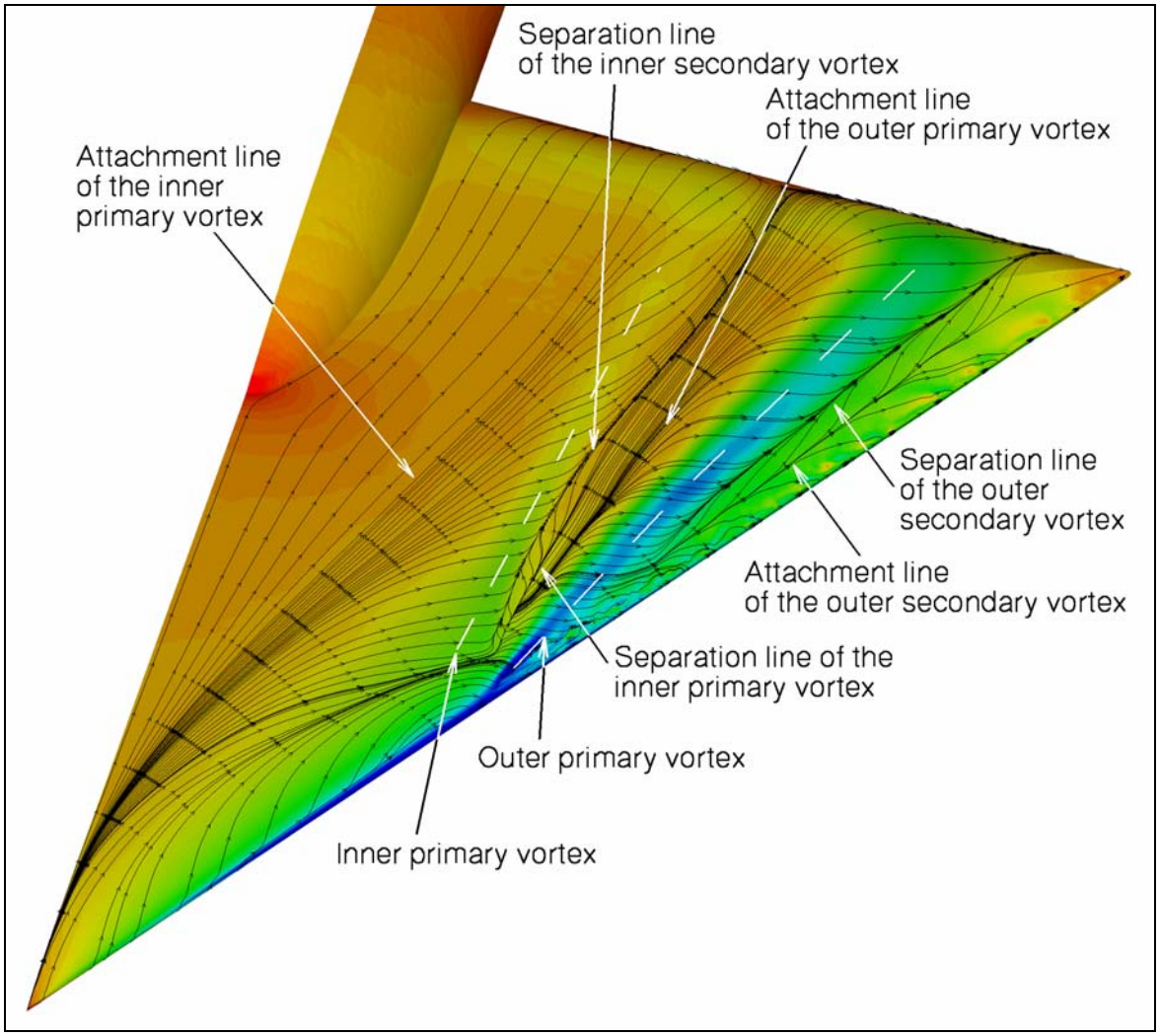

Figure 31-20: Friction Lines and Pressure Distribution on the Upper Surface of the Delta Wing. TAU calculation at M = 0.4, Re = 3 x 10^6, α = 13.3°.

Regarding the pressure distributions in Figure 31-20 as well as the results discussed before it is assumed that the flow around the leading edge is attached from the apex to the point were the inner vortex is generated. Looking at the pressure distribution in Figure 31-16 there is only a suction peak at the leading edge x/c_{ref} = 0.2 and no bump in the more inboard pressure distribution which is an advice for a vortical flow. It can be observed from the friction lines at the apex in Figure 31-20 that the flow is diverted outboard towards the

leading edge. Looking at the pressure distribution at $x/c_{ref} = 0.4$ in Figure 31-16 it can be observed from the experiments that the flow at the leading edge is still attached but there is a suction peak at $y/s = 0.65$ which indicates the onset of the inner vortex. This can be observed as well in the simulation results at $x/c_{ref} = 0.4$ and $y/s = 0.7$ but much weaker than in the experiment. This indicates that the inner vortex occurs first and afterwards the outer primary vortex.

In Figure 31-21 the vorticity distribution in x = const. slices are shown. An initial layer of high vorticity generated from the apex close to the boundary layer can be observed. This layer is getting thicker while moving downstream and turning outboard. Finally this high vorticity layer is the origin of the inner vortex. This is also visible by streamlines released from different positions within the boundary layer and close to the wall as seen in Figure 31-22.

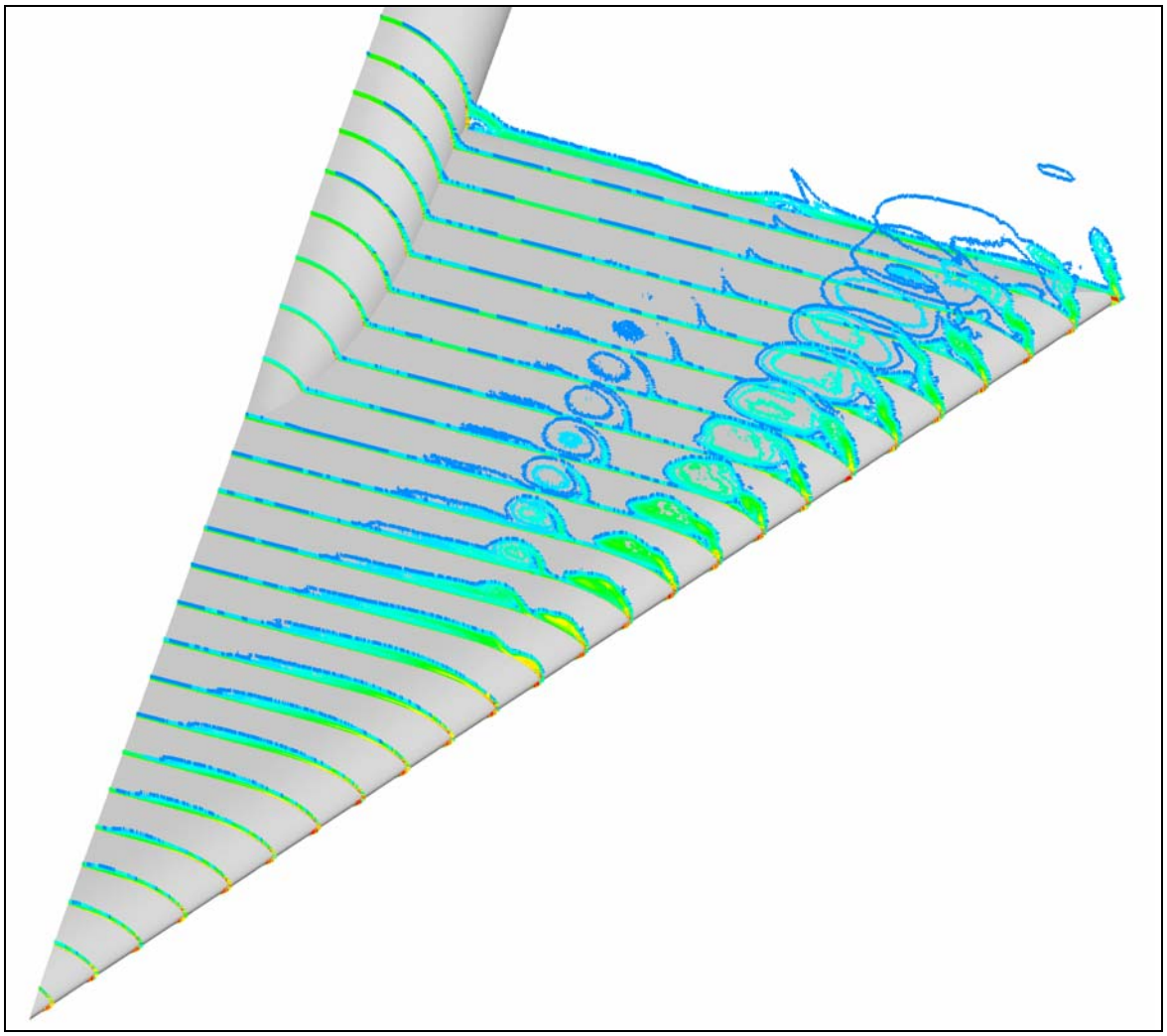

Figure 31-21: Vorticity Slices on the Upper Surface of the Delta Wing. TAU calculation at M = 0.4, Re = 3 x 10^6, α = 13.3°.

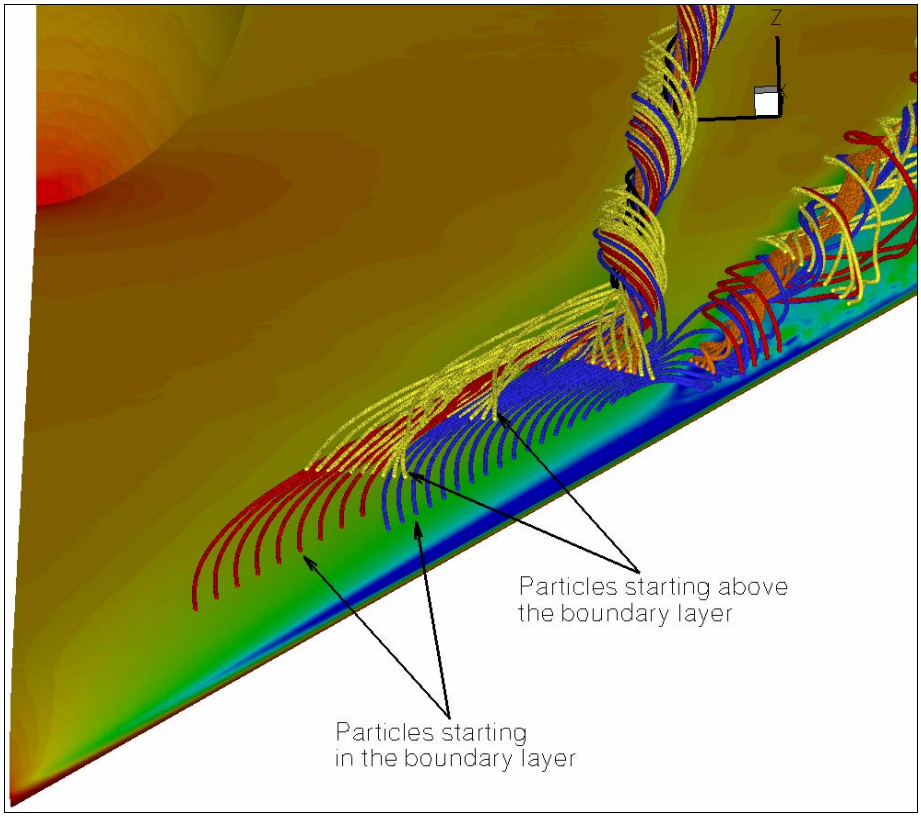

Figure 31-22: Streamlines and Pressure Distribution on the Upper Surface of the Delta Wing. TAU calculation at M = 0.4, Re = 3 x 10^6, α = 13.3°.

The red and blue traces start within the boundary layer flow. The flow is attached and strongly diverted outboard. It will finally feed the inner and outer primary vortex depending on the starting position. The yellow particles are starting out of the boundary layer within the high vorticity layer described before. These streamlines have a vorticity and generate a kind of vortex far upstream from the point where the outer vortex occurs.

Figure 31-23 supports this flow topology description by regarding the flow opposite to the free stream direction. It can be expected finally, that the inner vortex gets so much vorticity induced by the upstream vorticity layer where it hits the surface at the position where the outer primary vortex is generated, that it suddenly grows up in wall normal direction. The mechanism that forms the inner primary vortex might be directly related to the formation of the outer primary vortex. As seen in Figure 31-21 to Figure 31-23 the thin vorticity layer that represents the first stage of the inner primary vortex rolls up at the point where the outer primary vortex is generated. This behavior can be induced by the vorticity of the outer primary vortex.

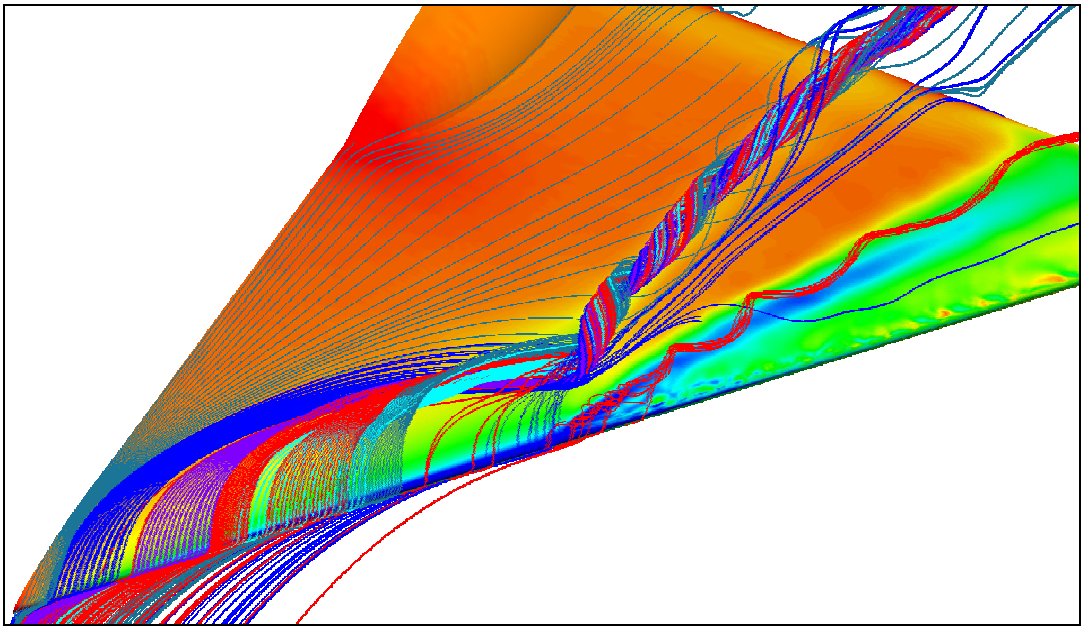

Figure 31-23: Streamlines and Pressure Distribution on the Upper Surface of the Delta Wing. TAU calculation at M = 0.4, Re = 3 x 10^6, α = 13.3°.

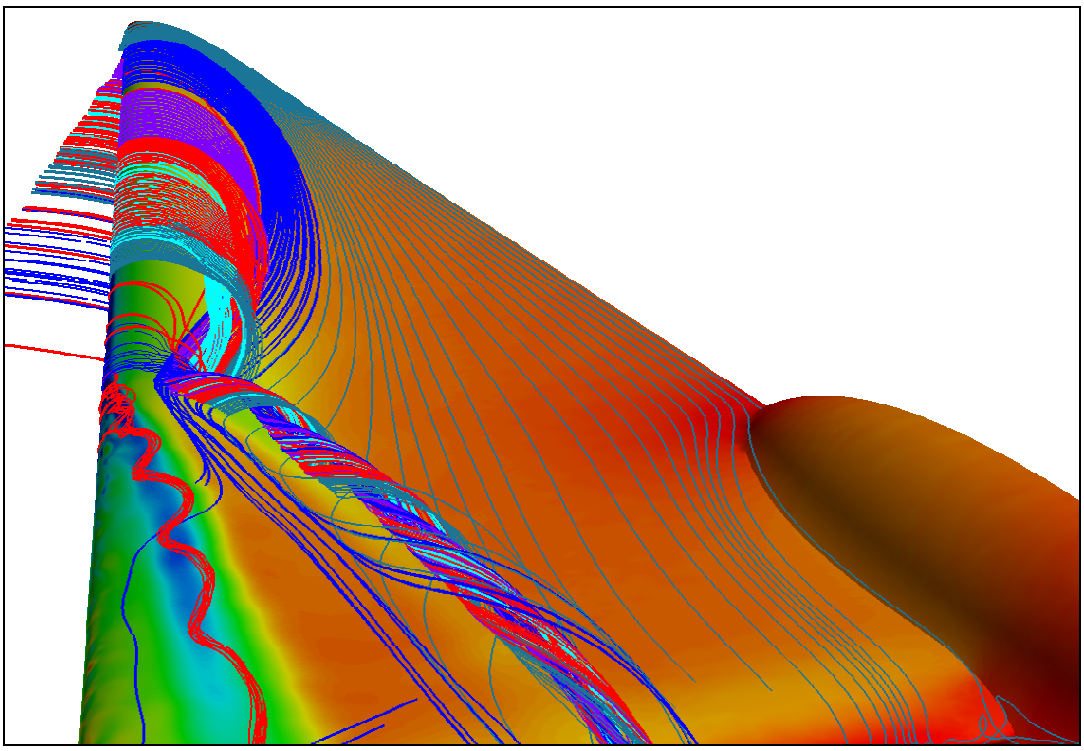

Figure 31-24: Streamlines and Pressure Distribution on the Upper Surface of the Delta Wing. TAU calculation at M = 0.4, Re = 3 x 10^6, α = 13.3°.

31.5 CONCLUSIONS

Results of CFD simulations using the DLR TAU-Code around a 65° delta wing with rounded leading edges at an angle of attack of α = 13.3° are presented in this chapter. The test case was chosen as an example for a complex flow topology with two primary vortices, an inner- and an outer one, instead of one vortex for the standard delta wing configuration with sharp leading edges. The DLR TAU-Code is a cell-vertex finite volume code using hybrid unstructured meshes. By means of simulations at the investigated angle of attack of 13.3° and at several different Reynolds numbers it is shown that the overall flow topology which is proven to be complex and sensitive with respect to various parameters can be predicted by this Code.

As demonstrated by the results a small increase of the angle of attack moves the position of the inner and outer vortex significantly more upstream. The main features of the flow field are carried out quite well by using the Spalart-Allmaras turbulence model. Nevertheless the inner vortex caused a weaker suction peak on the upper side of the delta wing and the outer vortex is generated too far upstream for this model approach. On the other hand the vortex is predicted further downstream than in the experiment by the Wilcox k-ω turbulence model. This model is furthermore very sensitive on the choice of the angle of attack. The influence of additional experimental boundary conditions like the wind tunnel walls are not taken into account within the presented investigations.

Although there are slight differences between the computed pressure distribution and the experimental data, several specific numerical and physical sensitivities are carried out. The influence of the turbulence model is taken into account by using two RANS models, the two equation Wilcox k-ω turbulence model and the one equation Spalart-Allmaras turbulence model. Influences of the Reynolds number and small changes in the incidence angle have been verified.

For all simulations fully turbulent flow is assumed which might be an inadequate simplification since it is not known from experiments whether or where transition occurs. Partly laminar flow at the leading edge may cause different separation behavior of the investigated vortices. This could lead to an earlier and stronger occurrence of the inner vortex. The generation of the outer vortex would be different as well in that case.

Finally the mechanisms of generating two primary vortices under the investigated flow conditions are discussed by means of the numerical simulation. It is shown that the inner vortex is generated out of a vorticity layer moving downstream and outboard towards the trailing edge, generating the inner vortex. It is also shown, that the inner vortex occurs earlier than the outer vortex.

31.6 REFERENCES

[31-1] Drougge, G.: *The International Vortex Flow Experiment for Computer Code Validation*, ICAS-Proceedings 1988, Vol. 1, pp. XXXV-XLI.

[31-2] Elsenaar, A., Hjelmberg, L., Bütefisch, K.-A. and Bannink, W.J.: *The International Vortex Flow Experiment*, AGARD-CP-437 (1988), Vol. 1, pp. 9-1 to 9-23.

[31-3] Wagner, B., Hitzel, S., Schmatz, M.A., Schwarz, W., Hilgenstock, A. and Scherr, S.: *Status of CFD Validation on the Vortex Flow Experiment*, AGARD-CP-437 (1988), Vol. 1, pp. 10-1 to 10-10.

[31-4] Hoeijmakers, H.W.M.: *Modeling and Numerical Simulation of Vortex Flow in Aerodynamics*, AGARD-CP-494 (1991), pp. 1-1 to 1-46.

[31-5] Luckring, J.M.: *Recent Progress in Computational Vortex-Flow Aerodynamics*, AGARD-CP-494 (1991), pp. 6-1 to 6-21.

[31-6] Hummel, D.: *Zur Umströmung scharfkantiger schlanker Deltaflügel bei großen Anstellwinkeln*, Z. Flugwiss, 15 (1967), 376-385.

[31-7] Hummel, D.: *Experimentelle Untersuchung der Strömung auf der Saugseite eines Deltaflügels*, Z. Flugwiss, 13 (1965), 247-252.

[31-8] Hummel, D.: *Effects of Boundary Layer Formation on the Vortical Flow Above Slender Delta Wings*, Proceedings of the I MECH E Part G Journal of Aerospace Engineering, Volume 220, Number 6, 2006, pp. 559-568(10).

[31-9] Hummel, D. and Redeker, G.: *A New Vortex Flow Experiment for Computer Code Validation*, RTO-AVT Symposium on "Vortex Flow and High Angle of Attack", Loen, Norway, 07-11.05.2001.

[31-10] Galle, M., Gerhold, T. and Evans, J.: *Technical Documentation of the DLR TAU-Code*, DLR-IB 233-97/A43 1997.

[31-11] Gerhold, T., Galle, M., Friedrich, O. and Evans, J.: *Calculation of Complex Three-Dimensional Configurations Employing the DLR TAU-Code*, AIAA-97-0167, 1997.

[31-12] Gerhold, T: *Overview of the Hybrid RANS Code TAU*, in N. Kroll, J. Fassbender (Eds.) MEGAFLOW – Numerical Flow Simulations for Aircraft, NNFM Vol. 89, Berlin, 2005, pp. 81-92.

[31-13] Centaur Soft: http://www.Centaursoft.com.

[31-14] Spalart, P.R. and Allmaras, S.R.: *A One-Equation Turbulence Model for Aerodynamic Flows*, AIAA-Paper 92-0439, 1992.

[31-15] Wilcox, D.C.: *Reassessment of the Scale Determining Equation for Advanced Turbulence Models*, AIAA-Journal, Vol. 26, No. 11, pp. 1299-1310, 1988.

[31-16] Chu, J. and Luckring, J.M.: *Experimental Surface Pressure Data Obtained on 65° Delta Wing Across Reynolds Number and Mach Number Ranges*, NASA Technical Memorandum 4645, Vol. 1-4, 1996.

[31-17] Konrath, R., Klein, C., Engler, R.H. and Otter, D.: *Analysis of PSP Results Obtained for the VFE-2 65° Delta Wing Configuration at Sub- and Transonic Speeds*, 44th AIAA Aerospace Sciences Meeting and Exhibit 9-12 January 2006, AIAA Paper No. 2006-60-592, Reno, Nevada.

[31-18] Klein, C., Sachs, W.E., Henne, U., Engler, R.H., Wiedemann, A. and Konrath, R.: *Development of PSP Technique for Application on the VFE-2 65° Delta Wing Configuration*, 44th AIAA Aerospace Sciences Meeting and Exhibit 9-12 January 2006, AIAA Paper No. 2006-59-624, Reno, Nevada.

[31-19] Konrath, R., Schröder, A. and Kompenhans, J.: *Analysis of PIV Results Obtained for the VFE-2 65° Delta Wing Configuration at Sub- and Transonic Speeds*, 24th Applied Aerodynamics Conference 5-8 June 2006, AIAA Paper No. 2006-3003, San Francisco, California.

[31-20] Boelens, O.J., Görtz, S., Morton, S., Fritz, W. and Lamar, J.E.: *Description of the F-16XL Geometry and Computational Grids Used in CAWAPI*, 45th AIAA Aerospace Science Meeting and Exhibit, 8-11 January 2007, AIAA Paper No. 2007-488, Reno, Nevada.